Mon. Not. R. Astron. Soc. **000**, 1–19 (1998) Printed 17 June 1998 (MN LATEX style file v1.4)

The Large-Scale HI Structure of the Small Magellanic Cloud

S. Stanimirovic,[1,2] L. Staveley-Smith,[2] J.M. Dickey,[3] R.J. Sault[2] and S.L. Snowden[4]
[1] *University of Western Sydney Nepean, P.O. Box 10, Kingswood, NSW 2747, Australia*
[2] *Australia Telescope National Facility, CSIRO, P.O. Box 76, Epping, NSW 2121, Australia*
[3] *University of Minnesota, 116 Church St. SE, Minneapolis, MN 55455, USA*
[4] *Code 662, NASA/Goddard Space Flight Center, Greenbelt, MD 20771, USA*

Accepted. Received; in original form

ABSTRACT
We combine new Parkes telescope observations of neutral hydrogen (HI) in the Small Magellanic Cloud (SMC) with an Australia Telescope Compact Array (ATCA) aperture synthesis mosaic to obtain a set of images sensitive to all angular (spatial) scales between 98 arcsec (30 pc) and 4° (4 kpc). The new data are used to study the HI spatial power spectrum over a range of contiguous scale sizes wider than those previously achieved in any other galaxy, including our own. The spatial power spectrum closely obeys the relation, $P(k) \propto k^{\gamma}$, with $\gamma = -3.04 \pm 0.02$, similar to values obtained by other authors for our own Galaxy which are in the range $\gamma = -3.0$ to -2.8. This is surprising given the very different morphology, gas-richness, star-formation rate and evolution of the two systems, and may imply similar mechanisms for structure formation. One interpretation of the $P(k)$ power-law is that the interstellar medium (ISM) of the SMC is fractal in nature, consisting of a hierarchy of HI cloud structures created, for example, by homogeneous turbulence. The projected fractal dimension of $D_p = 1.5$ is similar to values obtained by other authors for molecular clouds in the Galaxy in the size range ~ 0.05 to 100 pc. Such a model is consistent with a low space-filling factor for the neutral gas.

A kinematic study of the HI data reveals the existence of three supergiant shells which were previously undetectable in the ATCA data alone. These shells have diameters up to 1.8 kpc and require energies (in the standard supernova-driven models) up to 2×10^{54} erg. The structure and evolution of the ISM in the SMC is heavily influenced by the formation of these supergiant shells.

1 INTRODUCTION

The Small Magellanic Cloud (SMC) is a nearby dwarf irregular galaxy with low metallicity and a gas-rich interstellar medium (ISM) (Westerlund 1991). Being a part of the three-galaxy system that consists also of the Large Magellanic Cloud (LMC) and the Galaxy, the SMC has experienced a very disruptive history (Murai & Fujimoto 1980). An encounter with the LMC some 200 Myr ago is widely believed to be responsible for its present appearance (Gardiner, Sawa & Fujimoto 1994; Gardiner & Noguchi 1996). The line splitting observed in neutral hydrogen (HI) has been a subject of controversy, variously interpreted as expanding shells of gas or spatially separate systems (Hindman 1967; Mathewson, Ford & Visvanathan 1988; Martin, Maurice & Lequeux 1989; Staveley-Smith et al. 1997). Nevertheless, the SMC is an excellent laboratory for studying the inventory of the ISM and its characteristics because it is distant enough for all objects to be treated as having the same distance (~50–60 kpc)* , unlike in the Galaxy where distance determination is relatively uncertain. At the same time, it is near enough for radio and optical data to be obtained down to parsec and sub-parsec scales.

Neutral hydrogen (HI) is an important constituent of the cool ISM. It has been widely studied in galaxies of different morphological types. Features like shells, filaments, arcs, worms and chimneys appear to be general phenomena in gas-rich galaxies in particular (Heiles 1984; Brinks & Bajaja 1986; Braun 1997). These features can be described qualitatively, as can their relationship with the ISM and stellar population. They can also be described quantitatively through distribution functions – e.g. the spatial power spectrum (Crovisier & Dickey 1983; Green 1993). Such statistical descriptions give the hierarchy of scales on which HI

* Throughout this paper we assume a distance to the SMC of 60 kpc.

is present in the ISM and therefore allow us to place constraints on the structure and topology of the ISM.

Although different models for the characterisation of the intrinsic topology of the ISM have been presented for the last 20 yr (e.g. Spitzer 1978), the question of the topology of the ISM has not been regarded as significant from the astrophysical point of view. Suggestions of the possible fractal nature of many objects (Scalo 1985, 1987; Elmegreen & Falgarone 1996; Elmegreen 1997) changed that perception, as the physical properties of fractals can differ greatly from those of canonical smooth clouds. For example, an interstellar grain will cool much faster if its surface is rough, like a fractal (Pfenniger & Combes 1994). The photon leakage from large HII regions, one explanation for the presence of the diffuse Hα emission, depends greatly on the 'openness' of the region. Conversely, certain physical processes in the ISM, such as turbulence or self-gravity, can strongly determine the topology of the ISM.

A previous study of the SMC (Staveley-Smith et al. 1997, hereafter Paper I), has examined the HI structure over the whole SMC on scales from 28 pc to $\sim$ 600 pc using interferometer data from the Australia Telescope Compact Array† (ATCA). In this paper, we extend those observations by including single-dish HI data from the Parkes telescope, thus extending our sensitivity to structures with sizes up to $\sim$ 4 kpc. A description of new aspects of the ATCA data reduction is given in Section 2. The new Parkes observations are also presented here, for the first time. The different aspects of the short-spacing correction are briefly discussed in Section 3. The process of combining ATCA and Parkes data sets is outlined. The combined data-set together with a comparison with previous observations is presented in Section 4. In Section 5, we discuss HI self-absorption. In Section 6 we derive the spatial power spectrum for the SMC, compare results with similar work done for our Galaxy and discuss a fractal model of the ISM. We discuss three supergiant shells, revealed by including Parkes data, in Section 7.

2 OBSERVATIONS AND DATA REDUCTION

2.1 ATCA observations and reduction

The ATCA, a radio interferometer, was used to observe 320 overlapping fields containing the SMC in 1992 October 6–14. An area of 20 deg^2 was observed with 5 antennas in a 375-m, east-west array. Most data were reduced using the MIRIAD system (Sault, Teuben & Wright 1995) . The observations and data reduction are described more completely in Paper I. The velocity spacing was 1.65 km s^{-1} and the angular resolution was 98 arcsec (FWHM).

Some processing in addition to that described in Paper I was performed. In particular all daytime data taken during October 6 were removed to reduce solar interference. Also, continuum subtraction was redone using a higher velocity for the assumed range of line-free channels. These extra steps removed the four low-level artifacts in the north-east (noted in Paper I) due to the residual emission present in the previously assumed line-free velocity range.

† The Australia Telescope is funded by the Commonwealth of Australia for operation as a National Facility managed by CSIRO.

An imaging task was then used to form a linear mosaic image. Visibilities were robustly weighted (Briggs 1995), with a robust parameter equal to zero. The rms noise, measured in line-free parts of the final cube, is 22 mJy beam^{-1}. The corresponding 1-σ brightness temperature sensitivity is 1.4 K, or a column density sensitivity of 4.2×10^{18}cm^{-2} per 1.65 km s^{-1} channel. Note, however, that neither robust weighting nor uniform weighting (as used in Paper I) give optimum sidelobe suppression for mosaics (Sault, Staveley-Smith & Brouw 1996). Better suppression (and resolution) is achieved using 'super-uniform' weighting (Sault 1984; Sault, Staveley-Smith & Brouw 1996). However, for existing purposes, such weighting would increase the noise level to an rms of 2.7 K.

2.2 Parkes observations and reduction

Observations of the SMC were made with the 64-m Parkes telescope on 1996 March 14 – 17 and August 2 – 3. These data are presented here for the first time. A single-beam, cooled, 21-cm receiver was used to observe a total of 1540 pointings centred on RA 01$^{\rm h}$01$^{\rm m}$, Dec $-72°56'$ (J2000) and covering a total area of $4.5° \times 4.5°$ (which matches the ATCA coverage of Paper I). The telescope FWHP beamwidth is approximately 14.7 arcmin, and the pointings were spaced by 7.5 arcmin. An observing bandwidth of 8 MHz (1688 km s^{-1}) was used, and the AT correlator was configured to give 2048 channels on each of the two (linear) polarizations. This gives a channel spacing of 0.82 km s^{-1}, though consecutive channels were later averaged to give a channel spacing of 1.65 km s^{-1} to match the ATCA data. Although not presented in this paper, Galactic HI was also observed.

Data were taken by scanning the telescope in 35 tracks in declination (more strictly – the tangent plane y–axis), stopping at 44 discrete positions along each track, and integrating for 30 s at each position. After each declination track, a line-free calibration region at RA 00$^{\rm h}$10$^{\rm m}$, Dec $-60°00'$ (J2000) was observed. This was used for bandpass-removal. For calibration purposes, the highest brightness-temperature region in the SMC (pointing 416 at RA 00$^{\rm h}$47$^{\rm m}$52.6$^{\rm s}$, Dec $-73°02'19.8''$, J2000) was observed after each track. This was used to establish accurate relative calibration for the data on each day and in each polarization. Absolute calibration was based on observations of PKS B1934-638 which was assumed to have a flux density of 14.9 Jy at the observing frequency. With this calibration, pointing 416 has a peak flux density of 147.4 Jy, with an rms calibration accuracy of $\sim$ 0.7 per cent. This flux density is telescope- and feed-dependent, but contemporaneous observations of the Galactic calibration source S9 (T_B = 85 K, Williams 1973) gave a conversion factor to brightness temperature of 0.93 K Jy^{-1}, resulting in an estimated peak brightness temperature of 137 K for pointing 416‡. This is also the position of maximum HI column density in the SMC, for which a value of 1.14×10^{22} atoms cm^{-2} is measured. This corresponds to the extraordinarily high value, for any galaxy, of 91 M$_\odot$ pc^{-2} for the projected

‡ The theoretical conversion factor, based on a main-lobe beam area of 2.07×10^{-5} sr, is 0.78 K Jy^{-1}. The ratio represents a main-beam efficiency of $\sim$ 0.84.

surface density of neutral hydrogen alone. Results in Section 5 suggest that correction for self-absorption may increase this by ~ 1.44. For comparison with our results, Hindman (1967) quotes a peak brightness temperature of 150 K and his maps show a maximum HI column density of 1.28×10^{22} cm^{-2}. The spectra of McGee & Newton (1982) show a peak of 130 K, and a summation of their Gaussian decomposition gives a peak column density of 1.08×10^{22} cm^{-2}. The peak brightness temperature measured by Mathewson, Ford & Visvanathan (1986) is $\sim$ 150 K. All these temperatures and column densities appear to be within 15 per cent of our new values. We will return to the issue of column densities and the HI mass of the SMC later, following comparison with the ATCA data.

Observations of the continuum source PKS B0252-712 were also made after each declination scan. The average flux density of this was found to be 5.43 Jy, close to the 1992 ATCA value of 5.48 Jy. Observations of Hydra A gave flux densities almost identical to the Baars et al. (1977) value of 43.5 Jy (to which the 1934-638 flux-density scale is ultimately tied), if a beam-dilution factor of 1.08 is used to account for its non-compact nature (J.E. Reynolds, private communication).

The 2×1540 spectra were subsequently convolved onto a sky grid using a Gaussian convolving function with a FWHM of 12 arcmin. A North Celestial Pole (NCP) projection was used to match the ATCA projection. This broadened the angular resolution to 18.8 arcmin. A gridding correction factor (Sramek & Schwab 1989) of 1.63 was applied to account for the new beam size. This ensures that, as with the ATCA cube, a point source has a peak flux density equal to its true flux density.

3 THE SHORT-SPACINGS CORRECTION

There are two main approaches for combining single-dish and interferometer data: adding in the $u-v$ domain (Bajaja & van Albada 1979; Vogel et al. 1984), and adding in the image domain (Ye & Turtle 1991; Schwarz & Wakker 1991). The main disadvantage of the first approach for us is that the SMC is very extended and column densities are still significant at the edges of the region surveyed. Therefore edge-effects are significant when Fourier transforming to the $u-v$ domain. We therefore combined the data in the image plane. However, even after filling in the central hole in the $u-v$ plane with single-dish data, an interferometer's $u-v$ coverage will generally remain incomplete, and deconvolution will still be required. We chose to add the dirty maps together, and proceeded to deconvolve the resultant images using the combined beam. Cornwell (1988) and Sault et al. (1996) give convincing arguments for combining data before or during the deconvolution process.

3.1 Scaling factor

Before combination, an estimate of the relative calibration of the flux-density scales for the interferometer and the single-dish data is required. We define the calibration factor f as the ratio of the flux densities of an unresolved source in the single-dish and interferometer maps:

$$f = \frac{S_{\rm ATCA}}{S_{\rm Parkes}}. \tag{1}$$

Unfortunately, no suitable compact HI sources exist. However, a better way of determining this number is to compare flux densities in the region of overlap in the $u-v$ plane. This region should correspond to angular sizes to which both telescopes are sensitive.

An estimate of the ratio of the beam areas for the single dish and interferometer is also required:

$$\alpha = \frac{\Omega_{\rm ATCA}}{\Omega_{\rm Parkes}}. \tag{2}$$

A value $\alpha = 7.5\times10^{-3}$ was estimated from the square of the ratio of the 98-arcsec clean beam (Paper 1) and the convolved Parkes beam of 18.8 arcmin (Section 2.2).

To determine f we:

(i) apodised both the Parkes and ATCA images by multiplying by a function which smoothly decreased the image intensities to zero near the edges. This reduces edge effects, particularly for the Parkes image which has non-zero emission everywhere;
(ii) multiplied the Parkes cube by the beam area ratio, α;
(iii) Fourier transformed both dirty cubes, dividing the Parkes one by the Fourier transform of the Parkes beam;
(iv) calculated the ratio of the amplitudes of the ATCA and Parkes visibilities at all positions in the overlapping range of spatial frequencies (120λ–170λ) and for each velocity plane separately;
(v) estimated the modal value from a histogram of ratios for all velocity planes.

This gives

$$f = 1.05\pm0.05, \tag{3}$$

which is consistent with the relative calibration accuracy of both data sets. The adopted beam size of 18.8 arcmin for the effective Parkes beam gives a flux-density ratio independent of spatial frequencies (radii in the $u-v$ plane). This confirms our assumed value for α.

3.2 The Merging Process

The dirty-image cubes and the dirty-beam cubes (the ATCA beam varies with position) were then combined as follows:

$$I^D_{\rm comb} = (I^D_{\rm ATCA} + f\alpha I^D_{\rm Parkes})/(1+\alpha) \tag{4}$$

$$B_{\rm comb} = (B_{\rm ATCA} + \alpha B_{\rm Parkes})/(1+\alpha). \tag{5}$$

The combined dirty map was deconvolved with the combined cube of beams using MIRIAD's maximum-entropy algorithm (Sault et al. 1996). The model was restored with a 98-arcsec Gaussian. The rms noise of the combined cube, measured in an emission-free region is 21 mJy beam^{-1}. This corresponds to 1-σ brightness-temperature sensitivity of 1.3 K or a column-density sensitivity of 4.0×10^{18} cm^{-2} per 1.65-km s^{-1} channel. Including the calibration uncertainty coming from the f estimate, the final column-density sensitivity of the combined cube is 4.2×10^{18} cm^{-2} per 1.65-km s^{-1}channel.

A comparison was made with two other methods of image-plane combination. The first method uses the single-dish image as the 'default' image in the maximum-entropy

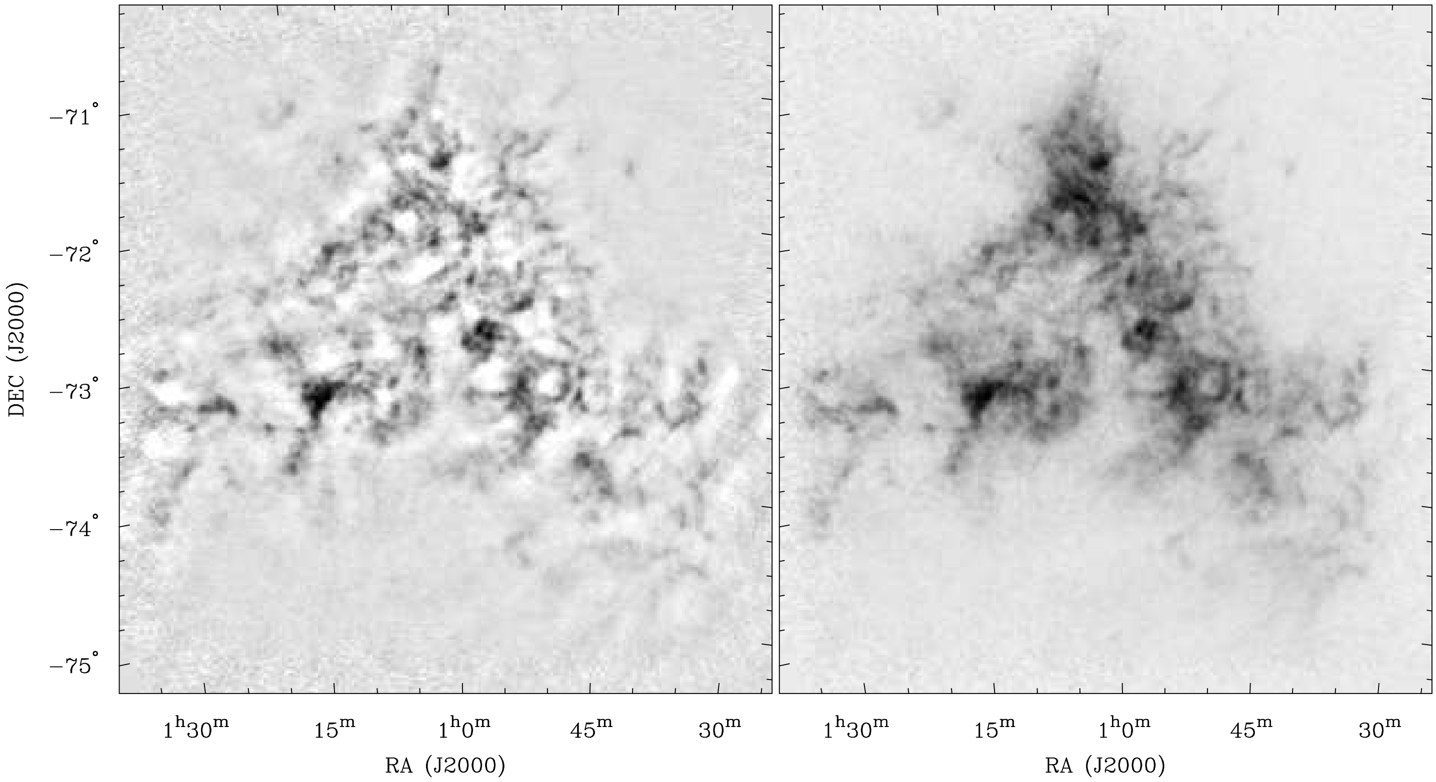

Figure 1. An HI image of the SMC at heliocentric velocity 169 km s^{-1} before (left) and after (right) adding the Parkes short-spacing data. The grey-scale intensity range is -11 to 87 K and -11 to 126 K, respectively. The beam size is 98 arcsec.

deconvolution procedure. In the absence of any other information or constraints, this forces the deconvolved image to resemble the single-dish image in the spatial frequency domain where the interferometer data contribute no information. The second method combines the images, after deconvolution of the ATCA image, in a similar manner to that already described. This is by far the easier way, but it does not allow the full $u-v$ information to be available to the deconvolver. A quantitative comparison of these methods will be published elsewhere (S. Stanimirović et al., in preparation). We found that rms noise and total flux for all three methods are roughly comparable. Image quality for the image combined before deconvolution appeared to be slightly superior, hence our decision to adopt this particular method. The same ATCA plane before and after adding short spacings is presented in Fig. 1.

4 DATA PRESENTATION

We present the data in the isovelocity images in Fig. 2. The cube was averaged for this purpose into 24 velocity planes, each of width 4.95 km s^{-1}. The figures have a grey-scale range from −0.18 to 2.0 Jy $beam^{-1}$ which corresponds to −11 to 126 K.[§] The maximum brightness temperature of the whole cube is 179 K at position RA $00^h48^m42^s$, Dec $-73°05'36''$ (J2000). This is the same position as, but 42 K brighter than, the maximum in the low-resolution Parkes data alone (Section 2.2), and 53 K brighter than the maximum in the ATCA data alone (Paper 1). At this position, the HI column density is 1.43×10^{22} atoms cm^{-2}, corresponding to 114 $M_\odot$ pc^{-2}, without correction for self-absorption. This is 25 per cent higher than that in the Parkes data alone.

The main difference between these data and those in previous single-dish studies is the complexity and variety of the small-scale structure. Much of this structure appears to be in the form of filaments, arcs, knots, and shells. Contrary to Hindman's description of a 'smooth HI distribution,' we see strong variation of the HI distribution spatially, and in velocity. At low velocities, the 'bar' is prominent (∼ 130 km s^{-1}) but, unlike the stellar bar, the HI bar is more extended and broken up into giant shells and supershells resulting from the interaction of the gas and the HII regions (see Section 6). An interesting drop of the total HI flux is present between 140 and 160 km s^{-1} (see also Fig. 6). At these velocities, the SMC appears to take on a 'wispy' morphology. A general velocity increase from west to east, seen on previous observations, is present and is partly caused by the parallax and the proper motion of the SMC. From the region of the bar, the SMC has three prominent extensions: (1) towards the north (∼ 160 km s^{-1}); (2) towards the Wing region in the south-east (∼ 160 km s^{-1}); and (3) towards the beginning of the Magellanic Stream in the north-east (∼ 190 km s^{-1}). The latter two were also noted by Bajaja & Loiseau (1982).

§ The conversion factor between flux density and brightness temperature is 63.07 K (Jy $beam^{-1})^{-1}$, the same as for the ATCA data alone.

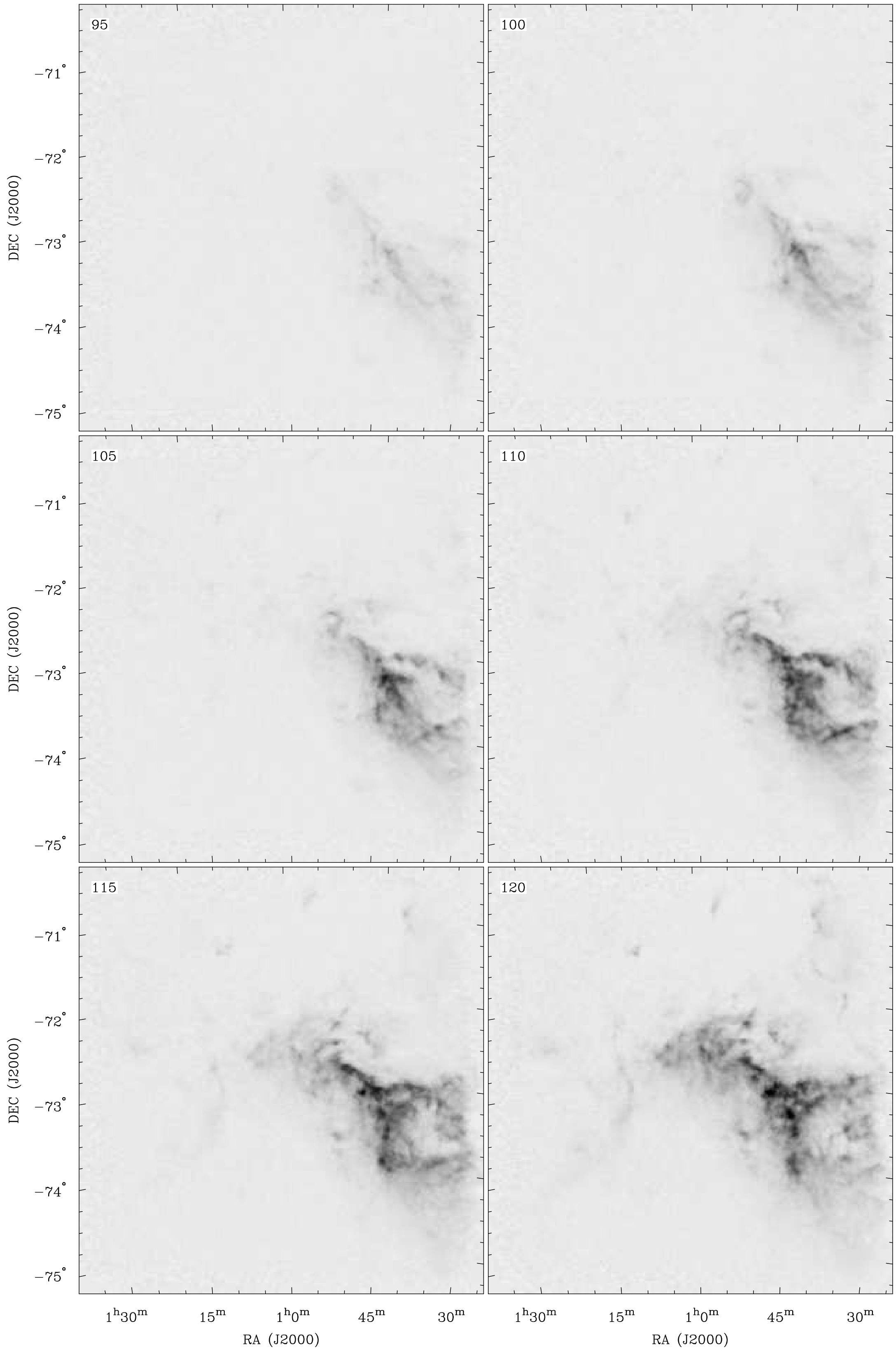

Figure 2. The combined ATCA and Parkes HI mosaic of the SMC. Each panel is an RA-Dec image for the heliocentric velocity given in the top-left corner. The velocity spacing is 4.95 km s^{-1}. The grey-scale intensity range is -11 to 126 K with a linear transfer function.

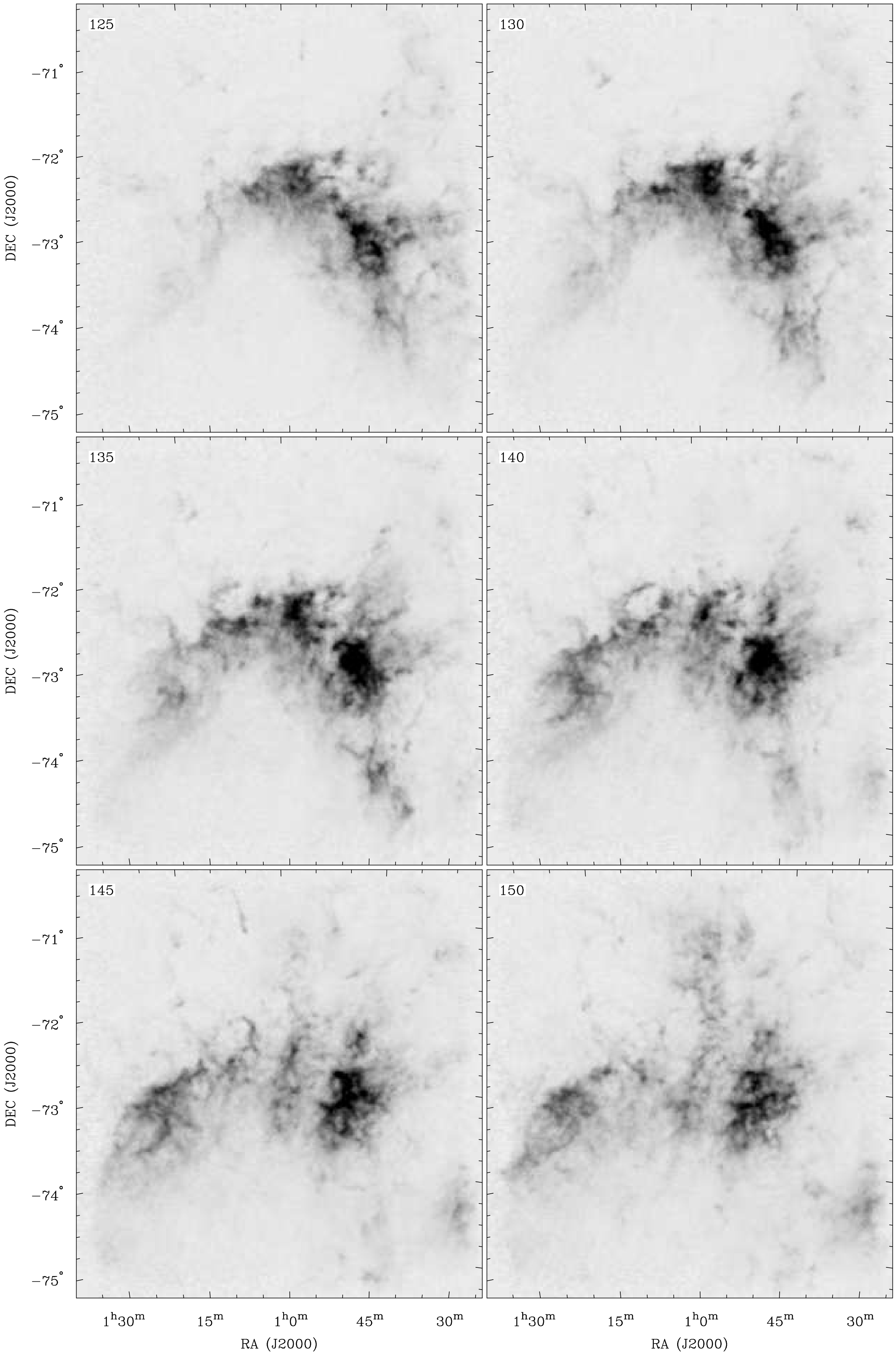

Figure 2 – *continued*

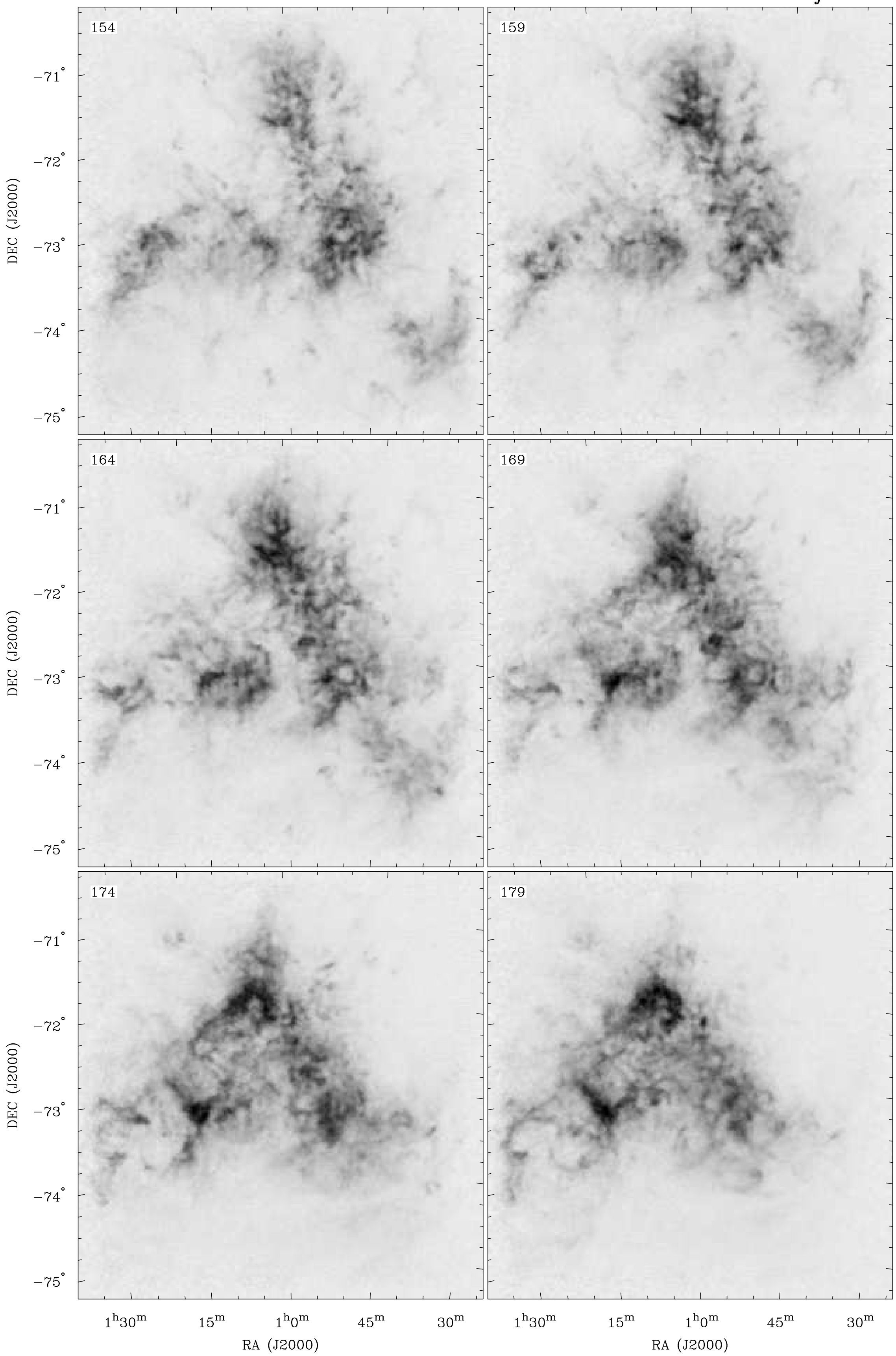

Figure 2 – *continued*

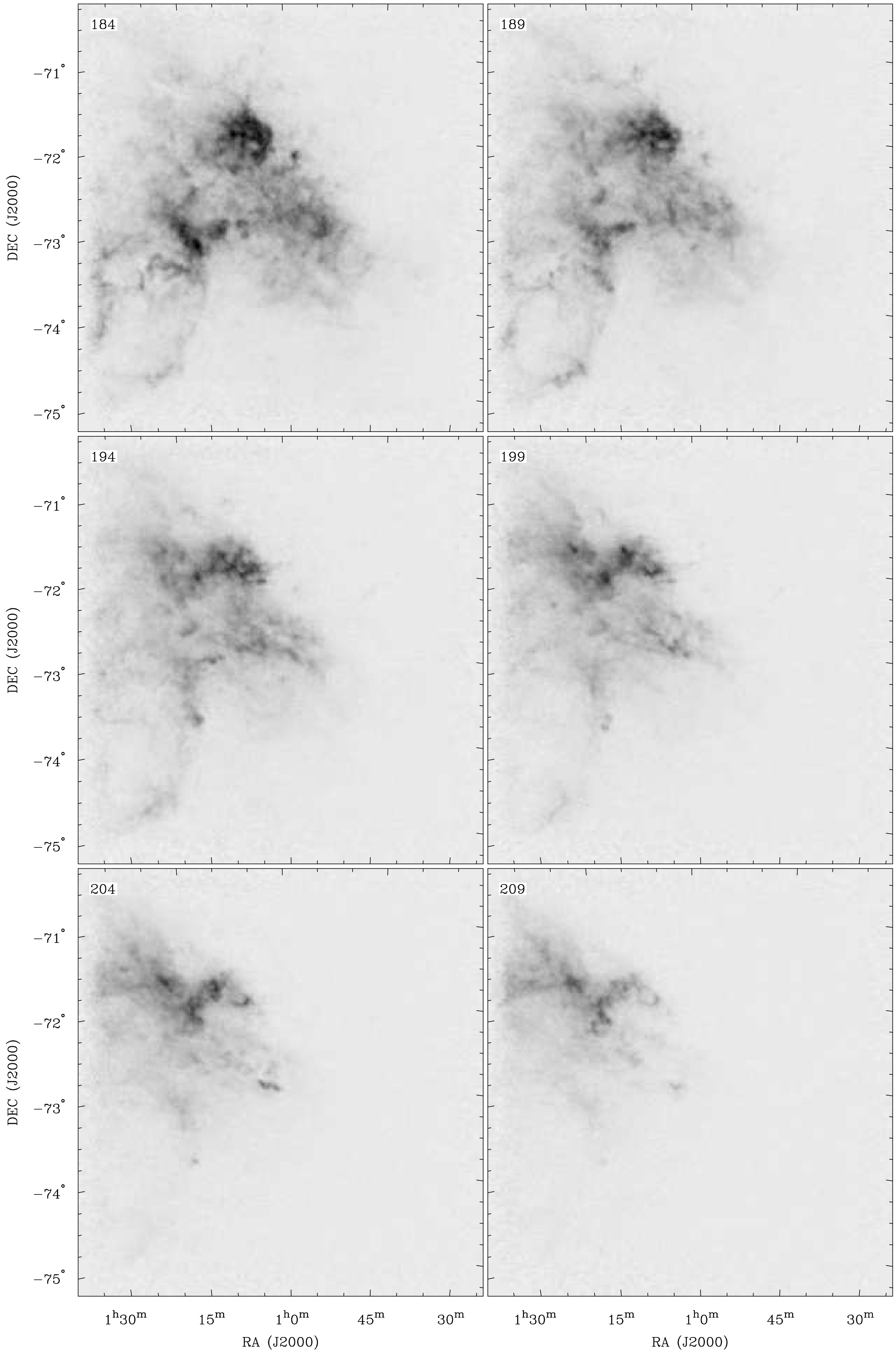

Figure 2 – *continued*

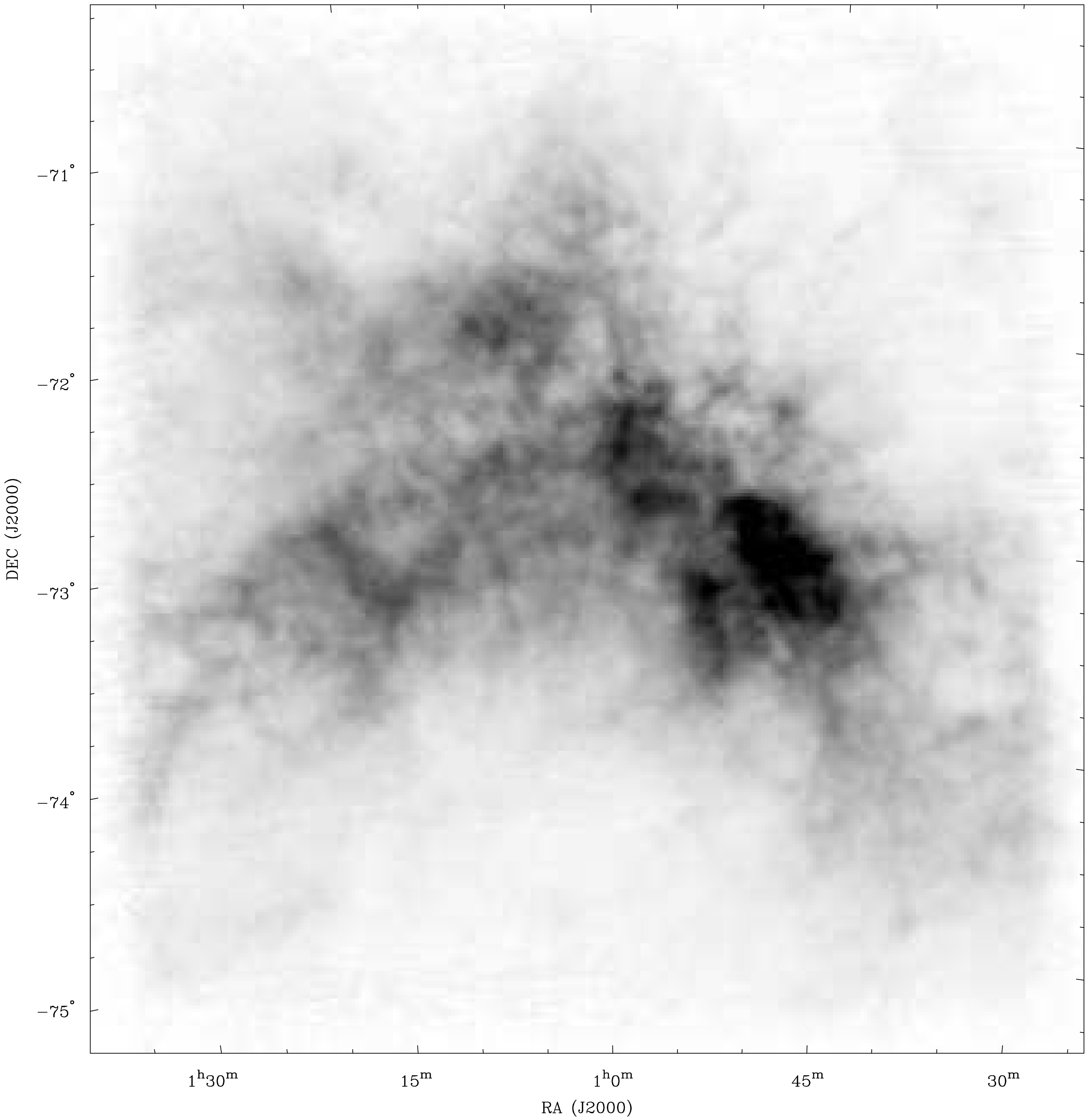

Figure 3. An HI column-density image of the SMC. The grey-scale intensity range is 0 to 1.03×10^{22} atoms cm^{-2} with a linear transfer function. The maximum HI column density, 1.43×10^{22} atoms cm^{-2}, is at position RA $00^{h}47^{m}33^{s}$, Dec $-73°05'26''$ (J2000).

As in Paper 1, a significant number of expanding supershells is apparent in the data. The largest of these shells are discussed in Section 7. Many of them have smaller shells on their perimeters, consistent with self-propagating star formation. In some cases (e.g. 145 km s^{-1}), several shells or filamentary structures appear to align into 'chimney'-like structures. A quantitative discussion of the relationship of large-scale and small-scale HI structure is given in Section 6.

The column-density image is shown in Fig. 3. The concentrations noted above remain visible, especially the bar, Wing and northern extension. A 'bridge' appears to connect the bar with the Wing. The overall filamentary structure of

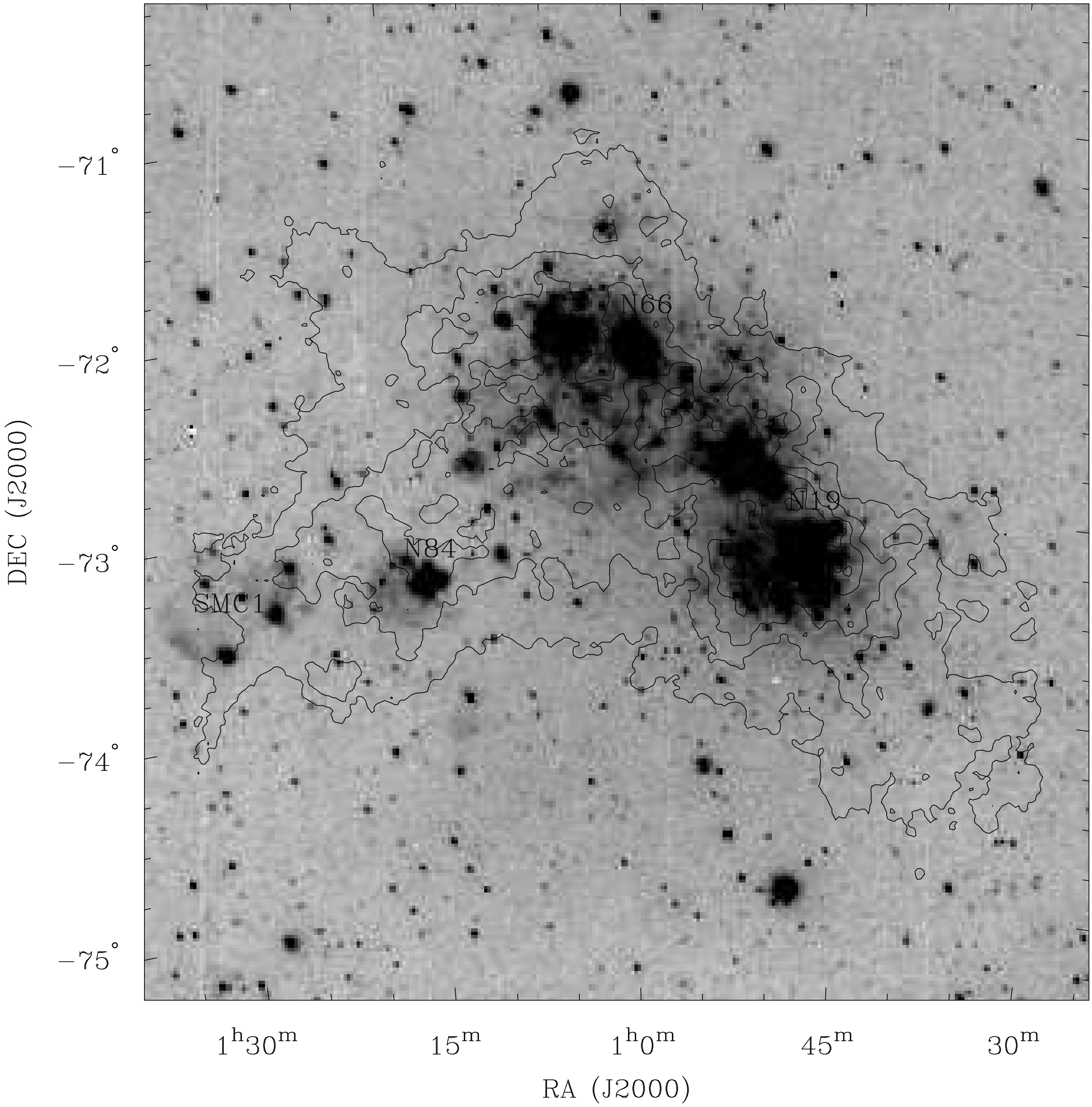

Figure 4. Contours of the HI column density overlaid on the Hα image of the SMC from Kennicutt et al. (1995). The contour interval is 5×10^{20} atoms cm^{-2} and contours are at 4, 6, 8 and 10 $\times$ contour intervals.

the SMC remains surprisingly visible – line-of-sight depth has not washed out much structure. Assuming low optical depth, we calculate a lower limit to the total HI mass in the observed area (see Section 2) of $(3.8 \pm 0.5) \times 10^8$ M$_\odot$. Hindman (1967) estimated the HI mass of a larger area, RA 00^{h}00^m to 01^{h}30^m and Dec $-70°$ to $-76°$ (B1975), to be slightly larger, 4.8×10^8 M$_\odot$. The total hydrogen mass of the area measured by Bajaja & Loiseau (1982) (RA 00^{h}00^m to 02^{h}00^m, Dec $-70°$ to $-76°$, B1950) is slightly higher still, $(5.5 \pm 0.4) \times 10^8$ M$_\odot$, after adjusting their assumed distance to 60 kpc. The main difference in our HI mass compared to that of previous authors appears to be the field of view. Calibration of the data sets appears to be consistent (c.f. Section 2.2).

Table 1. HI self-absorption corrections for different column density intervals in the SMC.

Column Density (10^{20} cm^{-2})	Area (deg^2)	Uncorrected HI Mass ($10^8 M_\odot$)	f_c	Corrected HI Mass ($10^8 M_\odot$)
< 25	18.3	1.35	1.0	1.35
25 to 65	0.62	1.89	1.1	2.08
65 to 100	0.85	0.50	1.3	0.65
> 100	0.11	0.10	1.5	0.15
Total	24.5	3.84		4.23

Fig. 4 shows contours of HI column density superimposed on an Hα image of the SMC from Kennicutt et al. (1995). The Hα image shows the prominent HII regions including N19 and N66 in the bar and N84A in the eastern Wing. The image also reveals two loop-like structures in the Wing – one associated with the N84A HII region and the other being the supershell SMC1 (Meaburn 1980). Extended Hα emission is also very prominent in the SMC and contributes about 36 - 46 per cent of the total Hα emission (Kennicutt et al. 1995). It consists mainly of diffuse emission associated with the bar, but there are prominent filaments which appear to stream towards the Wing. As Fig. 4 shows, both HI and Hα are most prominent in the bar. However, there is an absence of HI around the brightest HII regions as a result of star formation and stellar winds. A prominent example of this is N66 at RA $00^{\rm h}59^{\rm m}$, Dec $-72°11'$ (J2000). As noted previously, the HI extends beyond the diffuse Hα and the stellar bar, particularly towards the north and east. For the eastern wing, there is little general correlation between the Hα and the HI, although there is a tendency for HII regions to be near HI rims (see Section 7). For example, the V-shaped HI feature at RA $01^{\rm h}14^{\rm m}$, Dec $-73°12'$ (J2000) appears to be associated in position and velocity with N84A. The bridge which connects the stellar bar with the wing contains filamentary structure in both Hα and HI. However, there is little detailed correlation between the two. We discuss this further in Section 7.

5 HI SELF ABSORPTION

The column densities of atomic hydrogen determined here may be under estimates of the true column density if the gas is optically thick in the 21-cm line. In order to estimate the importance of this self-absorption effect, we have compared our data with the results of an absorption survey of the SMC by J.M. Dickey et al. (1998, in preparation). That project has observed some 30 lines of sight toward compact continuum sources behind the SMC, to measure the 21-cm optical depth as a function of velocity. Comparing those results with the corresponding emission spectra measured here, we can compute correction factors for the column densities measured when assuming low optical depth.

If we assume that the absorption lines measured by Dickey et al. represent gas at a single temperature, the combined data can be used to derive an average correction factor,

$$f_c = \begin{cases} 1 + 0.667\,(\log N_{\rm HI} - 21.4) & \log N_{\rm HI} > 21.4 \\ 1 & \log N_{\rm HI} \leq 21.4 \end{cases} \quad (6)$$

where $N_{\rm HI}$ is the column density in atoms cm^{-2}. Table 1 shows, for four different column-density ranges, the relevant area of the SMC, the uncorrected mass, the correction factor, and the corrected mass. Note that the lowest column density range (< 25) is a lower limit, since there is a lot of emission beyond our field of observation. The final result is that the self-absorption correction increases the HI mass estimate from 3.8×10^8 M$_\odot$ to 4.2×10^8 M$_\odot$. This is a relatively small effect. In individual velocity channels, the self-absorption correction can be much larger, as much as a factor of two in some cases, but typically the absorption covers only a narrow range of velocities compared with the emission, and so the effect on the velocity integral is relatively small.

6 SPATIAL POWER SPECTRUM

Following previous work in our own Galaxy by Crovisier & Dickey (1983) and Green (1993), we can now examine the power spectrum of the HI emission fluctuations in the SMC. With the ATCA and Parkes data combined, we are sensitive to fluctuations with angular sizes ranging from 1.6 arcmin to $\sim 4°$, or over 2 orders of magnitude. Moreover, as the distance to the SMC is well-established (we assume 60 kpc, ignoring any depth), angular size is directly related to physical size, unlike in our own Galaxy where distance determination is relatively uncertain. The corresponding range in linear size is 30 pc to 4 kpc.

The images, uncorrected for self-absorption, for a given velocity range were Fourier transformed. The average value of the square of the modulus of the transform, $< \Re^2 + \Im^2 >$, was then measured in 18 annuli of equal width in $\log\sqrt{u^2+v^2}$ (u and v are the coordinates in the Fourier plane, being measured in wavelengths, λ). As some parts of the Fourier plane corresponding to the ATCA data were not fully sampled (see Fig.2 in Paper I), we applied a mask. This mask excluded points outside the ellipse defining the longest baseline (semi-major axis $u = 2230\lambda$), and in three elliptical annuli of semi-major axes u = 730, 1440, and 1880λ, respectively.

Fig. 5 shows the two-dimensional spatial power spectra for six heliocentric velocity intervals 21.5 km s^{-1} wide. The spectra are remarkably well fitted by a power law, $P(k) \propto k^\gamma$ (k is in units of λ), over the whole linear size range. This implies that there is no preferred cloud size in the SMC. Because of the quality of the data set, the effects of noise and noise-bias (see Green 1993) are negligible. Unlike Green, and Crovisier & Dickey, we did not work directly in the observed uv-plane as our data were a combination of 320 ATCA fields and corresponding Parkes data for the whole region. Fig. 6 shows that the index of the power law is approximately constant over the full velocity range, with an average value being $< \gamma >= -3.04 \pm 0.02$. The average power at 1 kpc shows similar velocity structure to the integrated flux density profile (Fig. 6), although the lower velocity peak shows a higher level of emission fluctuations, despite its lower mass. Possibly, this is because of higher optical depth in the high-velocity component. After allowing for distance differences

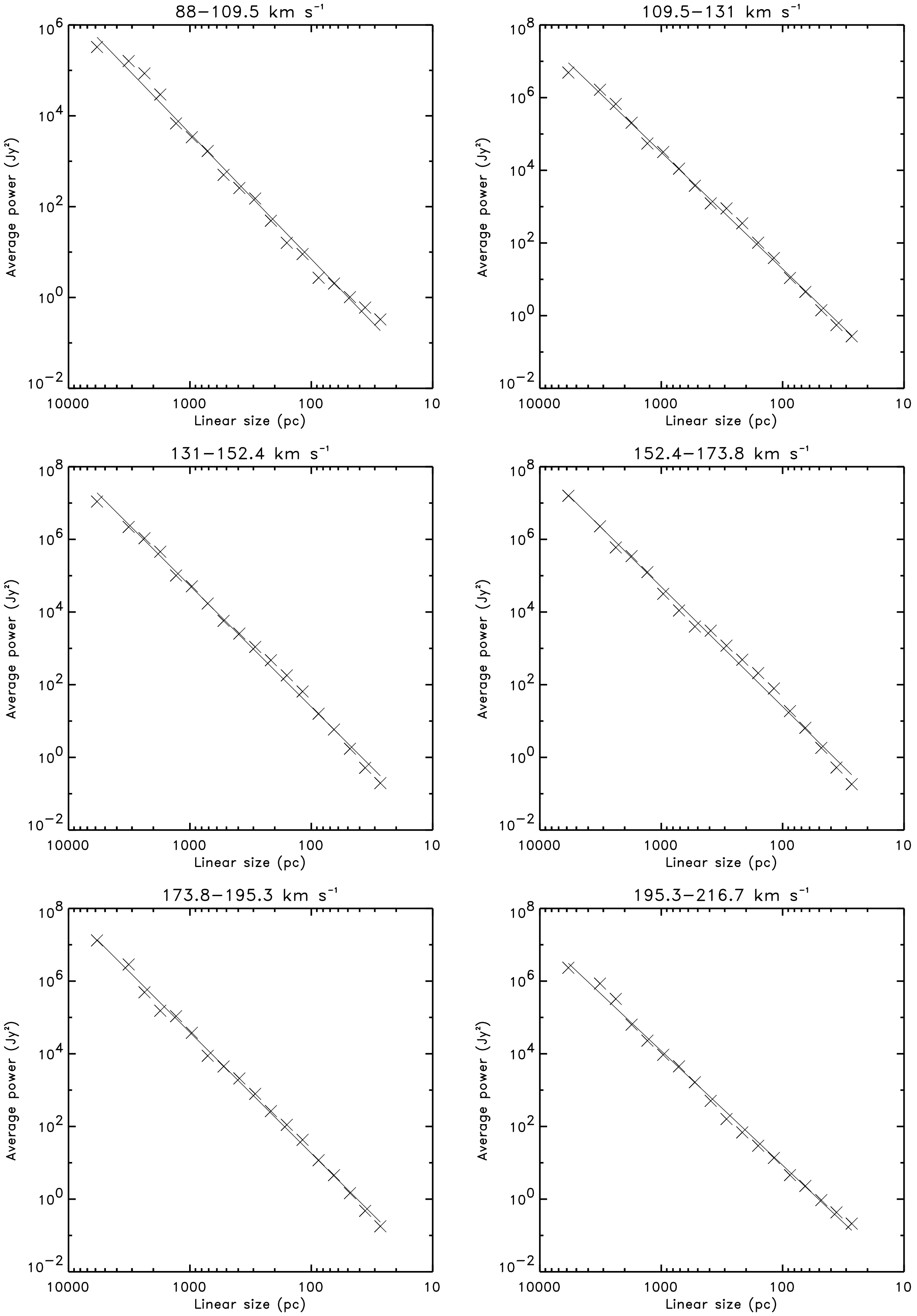

Figure 5. The two-dimensional spatial power spectrum for six heliocentric velocity intervals in the SMC. The linear size L, is related to the radius k in the uv-plane by $L(\mathrm{pc}) = d(\mathrm{pc})/k(\lambda)$, where $d = 60 \times 10^3$ pc is the distance to the SMC. Least-squares fits are overlaid.

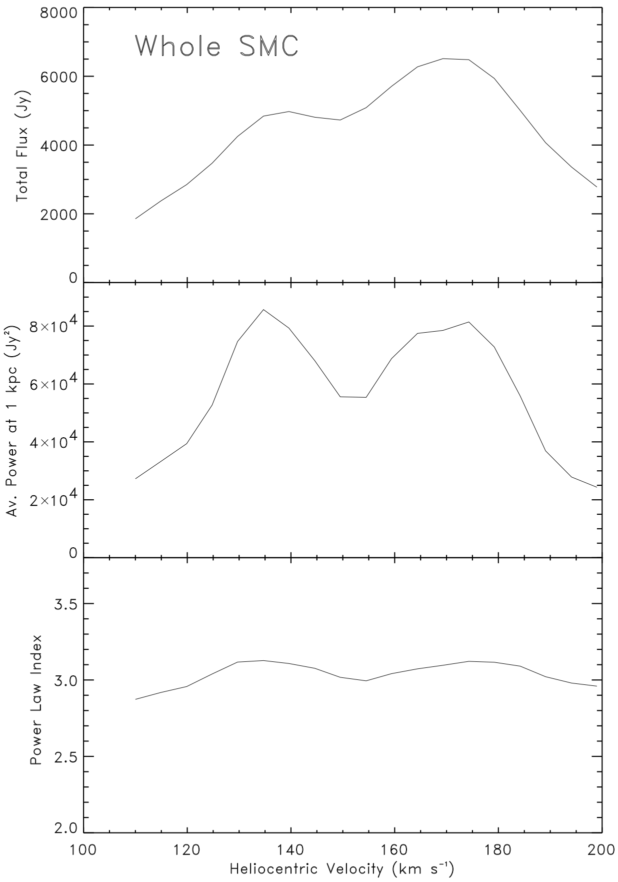

Figure 6. The total flux density in Jy (top), the average power at 1 kpc in Jy^2 (middle), and the slope of the 2-dimensional spatial power spectrum ($-\gamma$) of the whole SMC (bottom) plotted as a function of heliocentric velocity. The average slope is -3.04 ± 0.02.

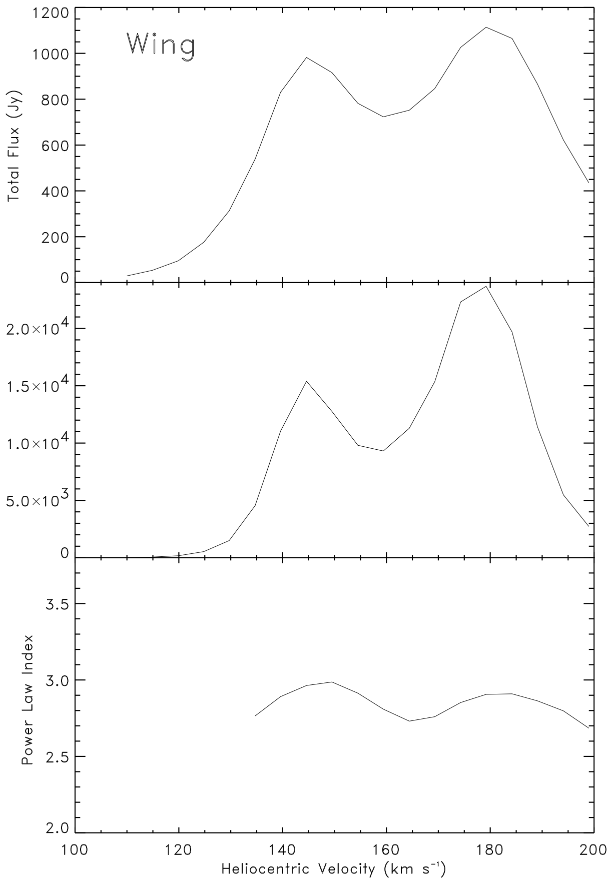

Figure 7. The total flux density in Jy (top), the average power at 1 kpc in Jy^2 (middle), and the slope of the 2-dimensional spatial power spectrum ($-\gamma$) of the eastern Wing (bottom) plotted as a function of heliocentric velocity. The average slope is -2.85 ± 0.02.

between the SMC and that part of the Galaxy studied by Green ($\sim$ 10 kpc) the power at 100 pc is higher in the SMC, as expected due to gas-richness. The velocity profile of the 100-pc power also follows the integrated flux-density profile. No discontinuity is seen at the transition ($\sim$ 420 pc) between the single-dish and interferometer data.

In order to test the two-dimensional spatial power spectrum in a smaller region of the SMC, we have applied the same method to the eastern Wing (area about 4 deg^2). Spectra are again very well fitted by a power law for the whole range of linear scale. In Fig. 7 we show the index of the power-law fit, together with the integrated flux density and the average power at 1 kpc. The average power at 1 kpc follows the total flux profile better, suggesting that this part of the SMC has lower optical depth. This provides more power on smaller scales and therefore a slightly lower average index, $<\gamma>=-2.85\pm0.02$.

For our own Galaxy, the interferometer data of Crovisier & Dickey (1983) and Green (1993) show power-law indices of -3.0 and -2.8, respectively. This implies that similar mechanisms are responsible for the HI emission fluctuations both in the Galaxy and in the SMC although the SMC is more gas rich and has a much younger environment.

At much smaller physical scales (below 0.2 pc), it was believed that emission fluctuations disappear in the Galaxy (Crovisier, Dickey & Kazes 1985). Extrapolation of the SMC power spectrum would also appear to suggest negligible emission fluctuations. At small scales, however, recent observations of absorption profiles against background continuum sources imply the presence of small dense HI clouds with a size of $\sim$ 75 AU in the Galaxy (Davis, Diamond & Goss 1996). Frail et al. (1994) also suggest that small-scale HI structure with a size range of 5 – 100 AU may constitute a significant fraction (10 to 15 per cent) of the cold neutral medium (CNM) in the ISM. If interpreted as density (rather than temperature) fluctuations, it therefore seems unlikely that this small-scale structure is related to the physical processes responsible for the hierarchy found here and may, for example, be related to a more local phenomenon such as shocks around individual low-mass stars.

Heiles (1997) also points out a 'pressure dilemma' whereby such small clouds appear to have very high thermal pressures compared with the equilibrium hydrostatic pressure of the ISM. He suggests an alternative geometric solution for the CNM in which very open filaments and sheets contribute about 30 and 10 per cent, respectively to the total column density of the CNM.

We note that there is a problem in studying the HI density fluctuations through emission–line observations in that we are not able to distinguish the warm and cold phases of the neutral hydrogen. The cold phase occupies a small fraction of the ISM whereas the warm phase filling factor is as much as $\sim$ 30 per cent in the Galaxy (Kulkarni & Heiles 1988). The warm-to-cold mass fraction in the Galaxy is ~ 3.2 (Dickey 1995), compared with 1.6, 2.0 and 4.6 for the galaxies M31, LMC and M33, respectively (Dickey 1995). Therefore, the spatial power spectrum in the SMC will also be biased towards the warm neutral medium (WNM), whereas absorption studies are biased toward the CNM.

6.1 A fractal origin for the spatial power spectrum?

Observations of interstellar clouds have shown that hierarchical structuring is present on a wide range of spatial scales. Some cloud properties, such as size distribution, mass distribution, density and velocity dispersion show distributions consistent with fractal structure (Elmegreen & Falgarone 1996). A similar inference can be made from the power-law nature of the HI spatial power spectrum.

Throughout, we assume the mathematical foundations of fractal geometry given by Falconer (1997). He refers to a set F as a fractal if:

(i) F has details over a large range of scale;
(ii) F is too irregular to be described in traditional geometrical language.

A fractal often has the following properties, in addition:

(iii) some form of self-similarity, approximate or statistical;
(iv) a 'fractal dimension' (defined in some way) which is greater than its topological dimension.

We use the fractal dimension D_H, given by Hausdorff (see Falconer 1997), which is smaller than or equal (for many sets) to the more popular box-counting or capacity dimension. For more information see Falconer (1997). The projection theorem says that the plane projection of a Borel set F (which Falconer uses as any subset of 3-dimensional Euclidean space, R^3) has a dimension equal to $D_p = \min\{2, D_H(F)\}$.

One of the usual manifestations of fractal structure (which is a fractal graph of the intensity distribution $I(\alpha, \delta)$ in this case) is that the power spectrum and correlation function of I show power-law behaviour (Falconer 1997). This leads to the possible interpretation of the power spectrum of the SMC as caused by fractal structure of the ISM in the SMC. The connection between the nature of the power spectrum and possible fractal structure was not made by Crovisier & Dickey (1983) nor Green (1993).

Following Falconer's discussion (Falconer 1997, p.158), the autocorrelation function, $C(L)$ (where L is the distance between two points or, here, a diameter of an HI cloud) of the fractal function is approximately a power-law:

$$C(L) \propto L^{4-2s}, \tag{7}$$

where s is the box-counting dimension of the graph of I. As the power spectrum, $P(k) \propto k^{\gamma}$ (k is in units of λ), is the Fourier transform of the autocorrelation function, we find $C(L)$ from:

$$C(\mathbf{L}) = \int\int P(\mathbf{k}) e^{i\mathbf{L}.\mathbf{k}} d\mathbf{k}. \tag{8}$$

As $k \propto L^{-1}$:

$$C(L) \propto \int k^{1+\gamma} dk \propto L^{-\gamma-2}, \tag{9}$$

where $< \gamma >= -3.04 \pm 0.02$. Hence, equating equations (7) and (9) we find that the box-counting dimension of the graph of I is 1.5 which is an upper limit for the projected Hausdorff dimension. Direct application of the projection theorem, assuming the whole ISM of the SMC to be a Borel set, gives an upper limit for the volume fractal dimension of 1.5. However, contrary to simple fractal models, the ISM presents a distribution of optical depths which will modify the relationship between the projected and volume dimension (Pffeniger & Combes 1994).

Similar results are obtained for the projected fractal dimension of interstellar clouds using the area-perimeter relationship (Falgarone, Phillips & Walker 1991). The results are remarkably similar for atomic, molecular and dust components of interstellar clouds and range between 1.3 and 1.4 (for references see Falgarone, Phillips & Walker 1991). Assuming the size distribution for substructures inside a fractal given with $N(\lambda > L) \propto L^{-D}$ (from Mandelbrot 1983), Elmegreen & Falgarone (1996) measure the volume fractal dimension of molecular clouds to be 2.3 ± 0.3 using data from published surveys.

The projected fractal dimension derived for HI in the SMC, $D_p = 1.5$, for structures present on scales from 30 pc to 4 kpc, is therefore very similar to the projected dimension derived for molecular clouds (Falgarone, Phillips & Walker 1991) with sizes from $\sim$ 0.05 pc to $\sim$ 100 pc. This may imply that the same mechanism causes the fractal structuring of all ISM components on all spatial scales.

The projected fractal dimension implies that the size distribution of substructures (on scales λ) greater than L will behave as $N(\lambda > L) \propto L^{-1.5}$, while the distribution of cloud size per linear size interval is given by $n(L)dL \propto L^{-2.5}dL$. Similarly, the mass–size relation obeys $M(L) \propto L^{1.5}$. These relations can be combined to give the cloud mass distribution function which is, interestingly, independent of fractal dimension: $n(M)dM \propto M^{-2}dM$ (Elmegreen & Falgarone 1996). Similar distributions have been derived for molecular clouds from CO observations (slope of -1.79) and for diffuse and IRAS clouds in the Galaxy (slope ranging between -1.5 and -2) (see Elmegreen & Falgarone 1996).

The fractal model of the ISM suggests highly inhomogeneous structure organization, different from any of the 'traditional' ISM models which have 1 or 2 levels of hierarchy. The dense regions of the ISM seem to be made of small and dense clouds ('atoms') and therefore are highly clustered, while the bulk of the ISM matter seems to have very low density (Elmegreen 1989). Different processes such as turbulence, chaos, self-gravity, percolation or some chemical processes can produce fractal structuring of an interstellar environment, even with similar fractal dimensions (Pfenniger & Combes 1994; Scalo 1987). However, analogies with laboratory fluids suggest that turbulence may have the most significant role in the ISM (Elmegreen & Falgarone 1996).

A future paper will discuss the expected intrinsic properties of HI clouds in a fractal ISM.

7 SHELLS

HI surveys of the Galaxy (Heiles 1979, 1984), M31 (Brinks & Bajaja 1986), M33 (Deul & den Hartog 1990), Ho II (Puche et al. 1992), the LMC (Kim et al. 1997) and other galaxies, show the presence of many giant and supergiant shells ($r \gtrsim$ 300 pc), as well as associated features such as filaments, incomplete shells, 'worms' and chimneys. This suggests that such features are probably a general phenomenon in gas-rich galaxies and fill appreciable fractions of the ISM. In the SMC, we have already catalogued 495 giant shells and 6 supergiant shells (Paper I).

Such features are explained by Bruhweiler et al. (1980) and Tomisaka, Habe & Ikeuchi (1981) as the evolution of an OB association in which an HI cavity is created by the strong stellar winds of massive stars. Elmegreen & Chiang (1982) show that, after a short time ($\gtrsim$ 3 Myr), the most massive stars become supernovae and the corresponding energy input can lead to runaway expansion and the formation of a supergiant shell. As the dynamic age of the largest observed supergiant shells is much greater than the time it takes for massive stars to evolve, big associations with $\sim$ 10^2–10^3 massive stars (McCray & Kafatos 1987) or regions of continuous formation and/or multiple formation of massive stars (Bomans et al. 1995) are needed to provide the shell with sufficient energy. One possibility for the latter is that star formation at one place can initiate star formation at another place, either by a stochastic process where the propagation is given with a certain probability (Gerola & Seiden 1978), or by a deterministic process where the propagation results from a chain of events (Palous 1996). If the expanding shell is located in a plane-stratified medium, it can expand upward forming a quasi-cylindrical or cone-like structure perpendicular to the disk (Tomisaka & Ikeuchi 1987; MacLow & McCray 1988). These 'HI chimneys' may be the source of the 'worm-like' features noted in our own Galaxy by Heiles (1984).

The hot gas retained inside the interstellar shells of young stars and supernovae is believed to be the sole source of the 'third-phase' of the ISM in galaxies (McKee & Ostriker 1977). Measuring the filling factor of the HI shells (the porosity parameter) therefore sets an important lower limit on the volume fraction of hot gas and gives an insight into ISM physics.

Another possible origin of supergiant shells is the collision of the infalling gas with gas in the Galactic Plane (Tenorio-Tagle 1981; Kulkarni & Heiles 1988).

Three supergiant shells in the SMC were noted by Hindman (1967). Meaburn (1980) later added another supergiant shell found on an Hα plate. Paper 1 lists a further six supergiant shells found using the ATCA data alone (and 495 giant shells). However, because of missing low spatial-frequency information, the sensitivity to the largest shells was very low. In this paper, we therefore re-examine the evidence for the very largest shells in the SMC.

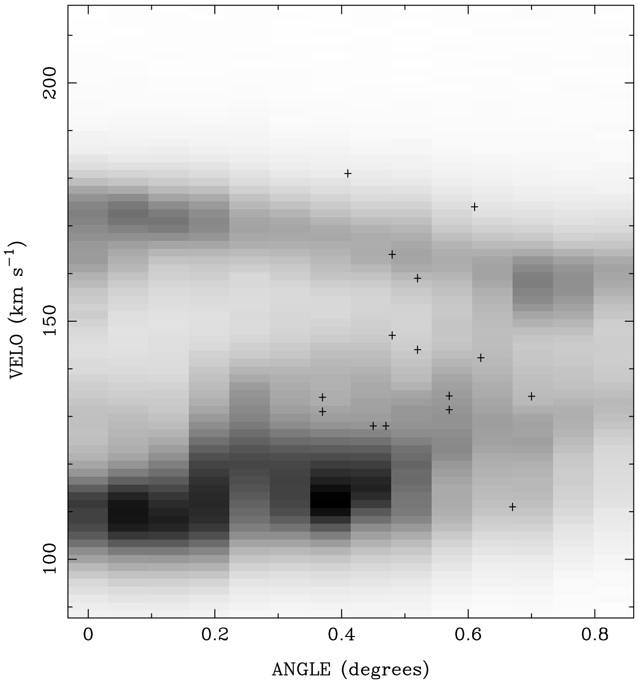

Figure 8. Radius–velocity plot for 37A SGS. For each velocity, the average radius of the emission from the centre of the shell is computed and ploted versus heliocentric velocity. The grey-scale intensity range is −3 to 69 K. Positions of some HII regions are overlaid (from Torres & Carranza 1987 and Smith & Weedman 1973).

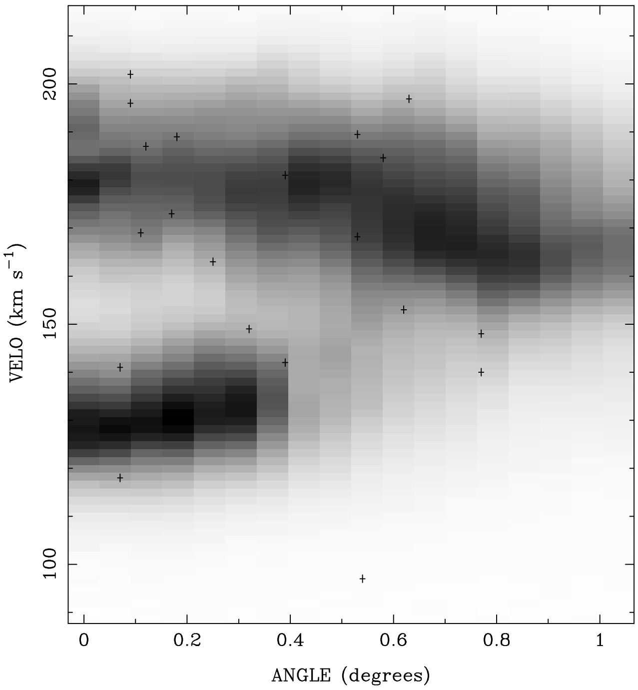

Figure 9. Radius–velocity diagram for 304A SGS. The grey-scale intensity range is −2 to 76 K. Positions of some HII regions are overlaid (from Torres & Carranza 1987 and Smith & Weedman 1973).

7.1 Properties of Three New Supershells

Inspection of the cube revealed three very large (radii $\gtrsim$ 600 pc) HI structures, each with the properties of an expanding supergiant shell (SGS). Each feature was visible in several successive position-velocity images as a partly complete el-

Table 2. Observed properties of the three supergiant shells with $r > 600$ pc in the SMC.

Supergiant Shell	RA (J2000)	Dec (J2000)	Heliocentric Velocity $V_{\rm hel}$ (km s^{-1})	Expansion Velocity v_s (km s^{-1})	Semi Axis Major (pc)	Minor (pc)	Position Angle ψ (°)	Surface Density σ ($M_\odot$ pc^{-2})
37A	00:40:26	-73:28:06	141	28	840	750	160	8.5
304A	01:02:16	-72:38:12	154	27	910	470	80	21.1
494A	01:27:18	-74:12:24	159	28	650	540	150	2.6

Table 3. Derived properties of the three supergiant shells with $r > 600$ pc in the SMC.

Supergiant Shell	Dynamical Age T ($10^7 yr$)	HI Mass $m_{\rm HI}$ ($M_\odot$)	Ambient Density n_0 (atoms cm^{-3})	Energy Required Φ (10^{53} erg)	SNs Required	Volume Factor f_v	Mass Fraction f_m
37A	1.7	3.3 $\times 10^7$	0.6	13.0	1×10^3	0.06	0.09
304A	1.4	5.7 $\times 10^7$	1.9	21.5	2×10^3	0.04	0.15
494A	1.2	5.6 $\times 10^6$	0.3	2.27	2×10^2	0.03	0.02

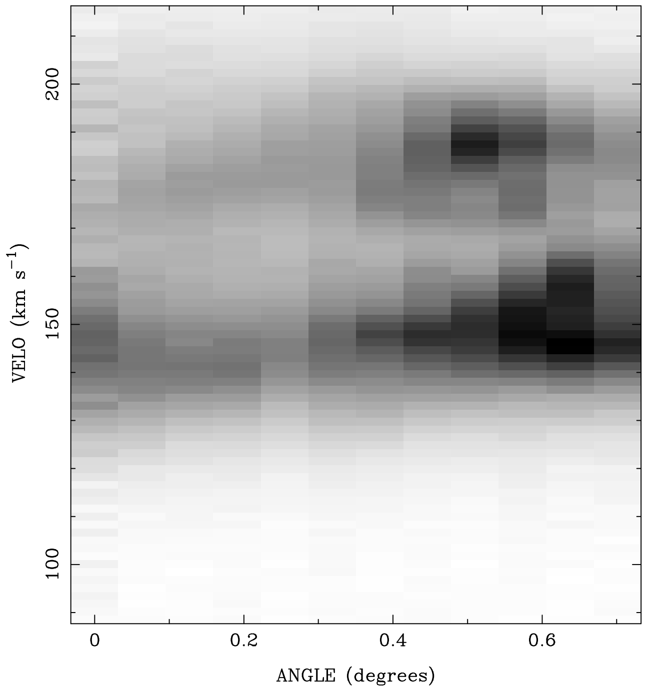

Figure 10. Radius–velocity diagram for 494A SGS. The grey-scale intensity range is -2 to 50 K.

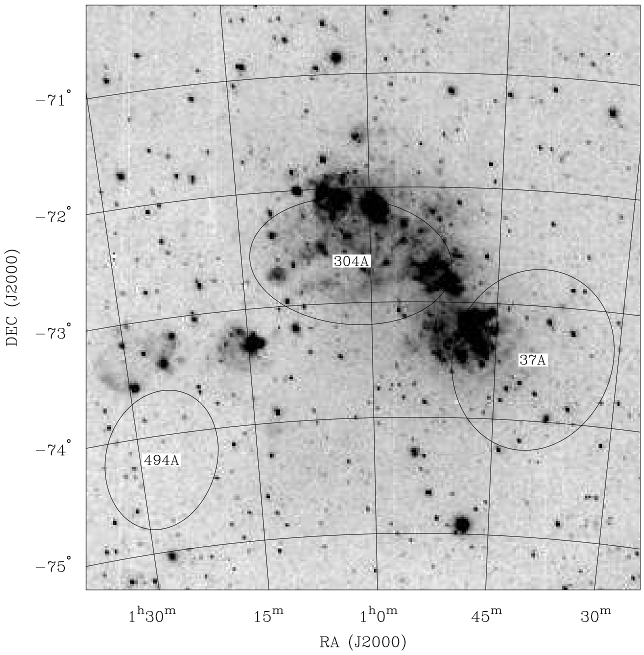

Figure 11. Positions of supergiant shells in the SMC superimposed on the Hα image from Kennicutt et al. (1995). A J2000 coordinate grid is overlaid. The position of each shell is given with an ellipse having shell's major and minor semi–axis and position angle.

lipse with a common centre. All three supergiant shells may consist of smaller interlocked or superimposed shells. Their rims often contain smaller shells, implying propagating star formation.

The expansion of the SGSs is shown in the radius-velocity plots shown in Fig. 8-10. In these plots, we show azimuthally averaged spectra as a function of radius from the centre of the shell. At small radii, the line of sight passes near the shell centre, and the highest blueshifts and red-shifts are seen. At larger radii, the radial velocities gradually approach the system velocity until the radius equals the maximum shell radius. For a thin spherical shell seen in projection, the observed velocity is given by

$$V = V_{\rm hel} \pm v_{\rm s}\sqrt{1-\left(\frac{\theta}{\theta_o}\right)^2} \quad (10)$$

where V is the observed velocity, θ is the projected radius, $V_{\rm hel}$ is the central shell velocity, θ_o is the shell radius, and $v_{\rm s}$ is the expansion velocity.

We overlay positions of some known HII regions (from Torres & Carranza 1987 and Smith & Weedman 1973) on the first two plots. The HII regions are more scattered in velocity than the HI, but nevertheless appear to avoid the shell interior. This suggests secondary star–formation.

In Table 2 we present the observed properties of these SGSs: identification, position (RA and Dec), central heliocentric velocity ($V_{\rm hel}$), expansion velocity (half the velocity separation of the peaks – $v_{\rm s}$), semi-major and semi-minor axes, position angle (ψ), and surface density (σ). All three SGSs were identified in both RA-velocity and Dec-velocity maps and the given position is an average of both measured positions. The major axis was measured in the plane containing the largest shell dimension. The surface density is the sum of the mean surface densities of both hemispheres measured using position–velocity maps. The final value is corrected for foreground and background gas, using the surface density measured near the central heliocentric velocity of each SGS.

The expansion velocities for all shells are similar, ~ 28 km s^{-1}. The semi-major axes range from 650 to 910 pc, and the surface densities (through both hemispheres) range from 2.6 M$_\odot$ pc^{-2} for 494A to 21.1 M$_\odot$ pc^{-2} for 304A. SGS 304A appears to have the most non-circular shape in projection (see Fig. 4).

The derived physical properties for each shell are given in Table 3: dynamical age (T), mass of the swept-up HI ($m_{\rm HI}$), average ambient density (n_0), energy input required (Φ), number of input supernovae required, volume fraction ($f_{\rm v}$) and HI mass fraction ($f_{\rm m}$). The total mass of the swept-up hydrogen was calculated from $m_{\rm HI} = 2\pi r^2\sigma$, where r is the geometric average of semi-major and semi-minor axes and σ is the surface density. Following the discussion by McCray & Kafatos (1987) on the evolution of a supergiant shell caused by an OB association, the main growth of a supergiant shell comes from combined effects of supernovae explosions. In the case of a large OB association, the rate of supernova explosion remains constant and the luminosity of a supergiant shell can be calculated from

$$\Phi = 1.5\times10^5\left(\frac{r}{100pc}\right)^5\left(\frac{T}{10^6yr}\right)^{-3}\left(\frac{n_0}{1{\rm cm}^{-3}}\right)L_\odot \quad (11)$$

(this equation is derived in the Paper I from equation 21 in Weaver et al. 1977). The dynamical age is obtained from $T = (3/5)(r/v_{\rm s})$. Assuming an average kinetic energy input per supernova of $\sim 10^{51}$ erg (McCray & Kafatos 1987), we calculate the number of supernovae required to produce these SGSs. The volume factor as the fraction of the SMC volume occupied by the shells is determined assuming 2 kpc for the radius of the SMC. The last column in Table 3 shows the fraction of the total SMC mass corresponding to each SGS.

All SGSs have significant expansion velocities compared to the SMC escape velocity of ≈ 50 km s^{-1}. This implies that a breakout from the main gaseous body of the SMC is possible.

7.2 Comparison with Previous Work

Two of the SGSs listed in Table 2 (37A and 494A) correspond to objects already catalogued in Paper 1 (SMC HI-10 and 491, respectively). Because of the large size of these shells, the current data supersede the previous data. Because of the change in measured position, the shell numbers have also changed. Thus SMC HI-10 and 491 no longer exist. The other SGS (304A) was not noted in Paper 1 because of its large size.

The spatial distribution of 495 giant shells in the SMC catalogued in Paper I shows that the two oldest shells are located in the south-west of the SMC. It is interesting to note that the oldest SGS, 37A, is also located in the south-west.

All three SGSs appear to be related to Hindman's (1967) shells. SGS 37A is 43 arcmin north from Hindman's second shell. The average radius is 45.4 arcmin, compared with Hindman's 45 arcmin. The central velocities and expansion velocities are slightly different: 141 km s^{-1} versus 129 km s^{-1} and 27.8 km s^{-1} versus 21 km s^{-1}, respectively. We measure the mass of swept-up HI to be 3.3 $\times10^7 M_\odot$, while Hindman measured 1.0 $\times10^7 M_\odot$.

The largest supergiant shell, 304A, appears also to correspond with Hindman's largest shell. The positions match remarkably well (within 7 arcmin). Central heliocentric velocities and expansion velocities are also very close: 154.5 km s^{-1} versus 160 km s^{-1} and 27.0 km s^{-1} versus 23 km s^{-1}, respectively. The HI mass is $\sim 6\times10^7 M_\odot$, while Hindman measured $2\times10^7 M_\odot$.

SGS 494A is $\sim$ 26 arcmin south from Hindman's third shell but with about the same average radius: 34 arcmin versus Hindman's 30 arcmin. Its central heliocentric velocity is 159.4 km s^{-1} versus Hindman's 160 km s^{-1} and expansion velocity is 28.2 km s^{-1} versus Hindman's 19 km s^{-1}. It is interlocked with SMC HI-491 and that could have caused some confusion in identifying it in previous observations. We measure $6\times10^6 M_\odot$ for the HI mass, while Hindman measures $3\times10^6 M_\odot$.

7.3 Supershells and the ISM

SGSs 37A and 494A appear to be reasonably uniform ellipses in position-velocity space, showing both hemispheres and with no apparent breakouts. Applying the theory of the supershell evolution (McCray & Kafatos 1987), they are most likely driven by $\sim 10^3$ and 10^2 supernovae (Table 2), respectively. However, SGS 304A is more complex, and much of the shell structure in the north is missing. This suggests that, if interpreted as an expanding SGS, the interior hot gas has vented out. The required energy (2.1×10^{54} erg), and therefore number of SNe ($\sim 2\times10^3$), is very large.

Positions of all three SGSs in the SMC are superimposed on an Hα image from Kennicutt et al. (1995) in Fig. 11. Two SGSs, 37A and 494A, have Hα emission on their rims, suggesting that their expansion stimulates new star formation. The other, SGS 304A, seems to be associated with the extended Hα emission in the north-east of the bar and has the bright HII regions, N66 and N36 on the northern perimeter, where the HI shell has a gap. All three SGSs appear to have reached an age ($> 10^7$ yr) when they do not produce enough ionising radiation to make visible any inner HII rims (McCray & Kafatos 1987). The HI and Hα filaments (see Section 4 and Fig. 4) seen near 304A may be associated with chimneys and outflow from the supershell. X–ray observations can give important constraints for the interpretation of these SGSs.

The derived properties, dynamical age, the HI mass and required energy, show that the largest SGSs in the SMC fit quite well into the population of SGSs discovered in other galaxies. For the Galaxy, M31, M33, IC10, M101 and NGC6946, the dynamical age varies from $\sim 10^7$ to 10^8 yr, mass from $\sim 10^7$ to 10^8 $M_\odot$ and energy from $\sim 10^{52}$ to 10^{54} erg (see review by van der Hulst & Kamphuis 1991). Compared with M31 and M33, the dynamic ages and sizes of the SGSs in the SMC are similar, but the HI masses and required energies are much higher. This is probably because of the SMC's very high ambient density. Compared with the Galaxy, SGSs in the SMC are all younger but have comparable masses and energies.

The volume fraction occupied by these three SGSs is 0.13 which, together with the volume fraction occupied by shells catalogued in Paper I (excluding SMC HI-10 and 491 which correspond to 37A and 494A, respectively), gives a total fraction of 0.3. In three-dimensional space, a volume factor of 0.3 implies a very 'bubbly' morphology. In the standard expanding shell model (Weaver et al. 1977), the interior is filled with hot gas. This therefore gives a lower limit of 0.3 for the volume factor of the hot gas in the SMC. This is somewhat lower than $\sim$ 0.7–0.8 predicted by the 'three–phase' ISM model of McKee & Ostriker (1977). Similar discrepancy has been already noticed in other galaxies (Brinks 1989). An alternative 'chimney' model of the ISM by Norman & Ikeuchi (1989) allows a two–phase model to change to a three–phase model with an increase in the SN rate. This model suggests that the galactic disk and halo are connected by chimneys which are consequences of superbubble breakouts from the disk. Chimneys bring hot gas into the halo and provide global mass and energy exchange between disk and halo. This model suggests 0.1 for the filling factor of the hot gas in the Galaxy, similar to the filling factor inferred for M31 by Brinks & Bajaja (1986). Given that the SMC is a much denser environment than the Galaxy, this model will require a higher specific SN rate than that required in the Galaxy.

The total volume factor $\Sigma f_v \approx 0.3$ of all shells in the SMC agrees extremely well with the prediction of Oey & Clarke (1997). Assuming standard adiabatic shell evolution and continuous star formation, Oey & Clarke derive the differential size distribution of OB superbubbles in a uniform ISM. They then derive the three–dimensional porosity parameter of 0.3 for the SMC. Such excellent agreement would imply, as stressed by Oey & Clarke, that the large–scale structuring of the ISM in the SMC is mostly determined by OB superbubbles and that no additional fundamental process is needed to explain the creation of the observed HI shells. However, their model assumes that most of the shells have stalled, contrary to the observations.

The mass fraction of the HI swept up by the largest SGSs, $\Sigma f_m \approx 0.26$ is somewhat greater than their filling factor, $\Sigma f_v \approx 0.13$, and implies that a substantial fraction of the total SMC mass is involved. This high mass fraction suggests that these large–scale features must have had an important role in the evolution of the SMC.

8 SUMMARY

In this paper, we have presented new Parkes telescope HI observations of the SMC. These have been combined with the existing Compact Array mosaic (which in turn was partly reprocessed) to produce an HI data cube which, for the first time, is sensitive to the full range of spatial scales between 30 pc and 4 kpc.

The new data set is used to reach the following conclusions regarding the topology and kinematics of the ISM in the SMC.

- The two-dimensional HI spatial power spectrum (which we have been able to measure over a range of contiguous scale sizes wider than those achieved in other galaxies) closely obeys the relation, $P(k) \propto k^\gamma$, with $<\gamma>= -3.04 \pm 0.02$. This is similar to values obtained by other authors for our own Galaxy, which is surprising given the very different morphology, gas-richness, star-formation rate and evolution of the two systems. This implies that similar mechanisms may be responsible for structure formation in both the Galaxy and the SMC.
- One possible interpretation of the $P(k)$ power-law is that the ISM of the SMC is fractal in nature, consisting of a hierarchy of HI cloud structures, created for example by homogeneous turbulence. We derive the corresponding projected fractal dimension of $D_p = 1.5$. Such a model implies a highly inhomogeneous ISM which is different from 'traditional' models which have 1 or 2 levels of hierarchy. Dense regions of the ISM would be made of clusters of dense and highly pressured 'clumps', while the bulk of the ISM matter would have very low density. Our results are similar to those obtained for molecular clouds with sizes ranging from $\sim$0.05 pc to 100 pc, suggesting that the same mechanism may produce fractal structuring on all spatial scales in the ISM.
- The new data set reveals the existence of three supergiant shells which were previously undetectable in the ATCA data alone. These shells have diameters ranging up to 1.8 kpc and appear to be related to those originally noted by Hindman (1967). We estimate the required energies (in the standard supernova-driven models) to produce such features and discuss their possible origin. The total filling factor of the known SMC shells is estimated to be 0.3 which is similar to the prediction of Oey & Clarke (1997).

The new SMC data set is available from the ATNF SMC web page (see http://www.atnf.csiro.au/research/smc_h1/).

ACKNOWLEDGMENTS

We thank Richard Gooch for helping with the karma visualisation software. We are grateful to Bryan Gaensler for beneficial discussions on the short-spacings correction. We also thank Raymond Haynes, Paul Jones and Graeme White for useful input to the paper. The papar has also benefited from comments made by internal referee Bärbel Koribalski.

REFERENCES

Baars J.W.M., Genzel R., Pauliny–Toth I.I.K., Witzel A., 1977, A&A, 61, 99B

Bajaja E., van Albada G.D., 1979, A&A, 75, 251
Bajaja E., Loiseau N., 1982, A&AS, 48, 71
Bomans D.J., Points S., Weis K., Chu Y.-H., 1995, RevMex-AASC, 3, 77B
Braun R., 1997, ApJ, 484, 637
Briggs D.S., 1995, Ph.D. thesis, New Mexico Institute of Mining and Technology
Brinks E., 1989, in Thronson, H.A., Shull, J.M., eds, The Interstellar Medium in Galaxies, (Kluwer Academic Publishers), p.39
Brinks E., Bajaja E., 1986, A&A, 169, 14
Bruhweiler F.C., Gull T.R., Kafatos M., Sofia S., 1980, ApJ Letters, 238, L27
Cornwell T.J., 1988, A&A, 202, 316
Crovisier J., Dickey J.M., 1983, A&A, 122, 282
Crovisier J., Dickey J.M., Kazes A., 1985, A&A, 146, 223
Davis R.J., Diamond P.J., Goss W.M., 1996, MNRAS, 283, 1105
Deul E.R., den Hartog R.H., 1990, A&A, 229,362
Dickey J.M., 1995, in Ferrara, A., McKee, C.F., Heiles, C., Schapiro, P.R., eds, The Physics of the Interstellar Medium and Intergalactic Medium, ASP conference series 80 (ASP: San Francisco)
Elmegreen B.G., 1989, ApJ, 344, 306
Elmegreen B.G., 1997, ApJ, 477, 196
Elmegreen B.G., Chiang W.–H., 1982, ApJ, 253, 666E
Elmegreen B.G., Falgarone E., 1996, ApJ, 471, 816
Falconer K., 1997, in Wiley J. & Sons Ltd, eds, Fractal Geometry, (Baffine Lane, England)
Falgarone E., Phillips T.G., Walker C.K., 1991, ApJ, 378, 186
Frail D.A., Weisberg J.M., Cordes J.M., Mathers C., 1994, ApJ, 436, 144
Gardiner L.T., Sawa T., Fujimoto M., 1994, MNRAS, 266, 567
Gardiner L.T. & Noguchi M., 1996, MNRAS, 278, 191
Gerola, H. & Seiden, P.E. 1978, ApJ, 223, 129
Green D.A., 1993, MNRAS, 262, 327
Heiles C., 1979, ApJ, 229, 533
Heiles C., 1984, ApJS, 55, 585
Heiles C., 1997, ApJ, 481, 193
Hindman J.V., 1967, Australian J. Phys., 20, 147
Kennicutt R.C., Bresolin F., Bomans D.J., Bothun G.D., Thompson I.B., 1995, AJ, 109(2), 594
Kim S., Staveley-Smith L., Sault R.J., Kesteven M.J., McConnell D., Freeman K.C., 1997, PASP, 14, 119
Kulkarni S.R., Heiles C., 1988, in Kellermann, K., Verschur, G.L., eds, Galactic and Extragalactic Radio Astronomy, (New York: Springer-Verlag), p.95
MacLow M., McCray R., 1988, ApJ, 324, 776
Mandelbrot B.B., 1983, in The Fractal Geometry of Nature, Rev. ed. of: Fractals. c1977 (New York: W.H. Freeman and Company)
Martin N., Maurice E., Lequeux J., 1989, A&A, 215, 219M
Mathewson D.S., Ford V.L., Visvanathan N., 1986, ApJ, 301, 664M
Mathewson D.S., Ford V.L., Visvanathan N., 1988, ApJ, 333, 617
McCray R., Kafatos M., 1987, ApJ, 317, 190
McGee, R.X., Newton, L.M. 1982. Proc. ASA, 4, 308
McKee C.F., Ostriker J. P., 1977, ApJ, 218, 148
Meaburn J., 1980, MNRAS, 192, 365
Murai T., Fujimoto M., 1980, PASJ, 32, 581
Norman C.A., Ikeuchi S., 1989, ApJ, 345, 372
Oey M.S., Clarke C.J., 1997, MNRAS, 289, 570
Palous J., 1996, in Blitz L. & Teuben P., eds, Unsolved problems of the Milky Way, IAU Symp. 169, Kluwer Academic Publishers (Dordrech/Boston/London)
Pfenniger D., Combes F., 1994, A&A, 285, 94
Puche D., Westpfahl D., Brinks E., Poy J.-R., 1992, AJ, 103, 1841
Reynolds J.E. private communication
Sault R.J., 1984, VLA Scientific Memo 154, NRAO Socorro
Sault R.J., Teuben P.J., Wright M.C.H., 1995, in Shaw R.A., Payne H.E., Hayes J.J.E., eds, Astronomical Data Analysis Software and Systems IV, ASP conference series 77, (ASP: San Francisco), p. 433
Sault R.J., Staveley-Smith L., Brouw W.N., 1996, A&AS, 120, 375
Scalo J.M., 1985, in Black D.C. & Matthews M.S., eds, Protostars and Planets II, (Tucson: Univ. Arizona Press)
Scalo J.M., 1987, in Hollenbach, D.J. & Thonson, H.A., eds, Interstellar Processes, (D. Reidel Publishing Company)
Schwarz U.J., Wakker B.P., 1991, in Cornwell, T.J., Perley, R.A., eds, Radio Interferometry: Theory, Techniques and Applications, IAU Colloq. 131, ASP conference series 19, (ASP: San Francisco)
Smith M.G., Weedman D.W., 1973, ApJ, 179, 461
Spitzer L.Jr., 1978, in Physical Processes in the Interstellar Medium (New York: Wiley)
Sramek R.A., Schwab F.R. 1989. in Perley, R.A., Schwab, F.R., Bridle, A.H., eds, Synthesis Imaging in Radio Astronomy, ASP conference series 6 (ASP: San Francisco)
Staveley-Smith L., Sault R.J., Hatzidimitriou D., Kesteven M.J., McConnell D., 1997, MNRAS, 289, 225
Tenorio-Tagle G., 1981, A&A, 94, 338
Tomisaka K., Habe A., Ikeuchi S., 1981, A&AS, 78, 273T
Tomisaka K. & Ikeuchi S., 1987, Pub. Astr. Soc. Japan, 38, 697
Torres G., Carranza G.J., 1987, MNRAS, 226, 513
van der Hulst T., Kamphuis J., 1991, in The Interstellar disk-halo connection in galaxies, AB (Groningen State Univ., Netherlands), p.201
Vogel S.N., Wright M.C.H., Plambeck R.L., Welch W.J., 1984, ApJ, 283, 655V
Weaver R., McCray R., Castor J., Shapiro P., Moore R., 1977, ApJ, 218, 377
Westerlund B.E., 1991, in Haynes R.F., Milne D.K., eds, Proc IAU Symp. 148, The Magellanic Clouds. Kluwer, Dordrecht, p.15
Williams D.R.W., 1973, A&AS, 8, 505
Ye T., Turtle A.J., 1991, MNRAS, 249, 722